

# **SANDIA REPORT**

SAND98-0510 • UC-810

Unlimited Release

Printed March 1998

## **High-G Accelerometer for Earth-Penetrator Weapons Applications**

### **LDRD Final Report**

Brady R. Davies, Stephen Montague, Vesta I. Bateman, Frederick A. Brown,  
Rajen Chanchani, Todd Christenson, James R. Murray, Danny Rey, David Ryerson

Prepared by  
Sandia National Laboratories  
Albuquerque, New Mexico 87185 and Livermore, California 94550

Sandia is a multiprogram laboratory operated by Sandia Corporation,  
a Lockheed Martin Company, for the United States Department of  
Energy under Contract DE-AC04-94AL85000.

Approved for public release; further dissemination unlimited.



**Sandia National Laboratories**

Issued by Sandia National Laboratories, operated for the United States Department of Energy by Sandia Corporation.

**NOTICE:** This report was prepared as an account of work sponsored by an agency of the United States Government. Neither the United States Government nor any agency thereof, nor any of their employees, nor any of their contractors, subcontractors, or their employees, makes any warranty, express or implied, or assumes any legal liability or responsibility for the accuracy, completeness, or usefulness of any information, apparatus, product, or process disclosed, or represents that its use would not infringe privately owned rights. Reference herein to any specific commercial product, process, or service by trade name, trademark, manufacturer, or otherwise, does not necessarily constitute or imply its endorsement, recommendation, or favoring by the United States Government, any agency thereof, or any of their contractors or subcontractors. The views and opinions expressed herein do not necessarily state or reflect those of the United States Government, any agency thereof, or any of their contractors.

Printed in the United States of America. This report has been reproduced directly from the best available copy.

Available to DOE and DOE contractors from  
Office of Scientific and Technical Information  
P.O. Box 62  
Oak Ridge, TN 37831

Prices available from (615) 576-8401, FTS 626-8401

Available to the public from  
National Technical Information Service  
U.S. Department of Commerce  
5285 Port Royal Rd  
Springfield, VA 22161

NTIS price codes  
Printed copy: A03  
Microfiche copy: A01



# High-G Accelerometer for Earth-Penetrator Weapons Applications LDRD Final Report

Brady R. Davies and Stephen Montague  
Intelligent Micromachines Department

Vesta I. Bateman and Frederick A. Brown  
Manufacturing and Rapid Prototyping Department

Rajen Chanchani  
Advanced Packaging Department

Todd Christenson  
Electromechanical Engineering Department

James R. Murray  
Digital ASICs Department

Danny Rey and David Ryerson  
Telemetry Technology Development Department

Sandia National Laboratories  
P.O. Box 5800 MS 1080  
Albuquerque, New Mexico 87185-1080

## Abstract

Micromachining technologies, or Micro-Electro-Mechanical Systems (MEMS), enable the development of low-cost devices capable of sensing motion in a reliable and accurate manner. Sandia has developed a MEMS fabrication process for integrating both the micromechanical structures and microelectronics circuitry of surface micromachined sensors, such as silicon accelerometers, on the same chip. Integration of the micromechanical sensor elements with microelectronics provides substantial performance and reliability advantages for MEMS accelerometers.

A design team at Sandia was assembled to develop a micromachined silicon accelerometer capable of surviving and measuring very high accelerations (up to 50,000 times the acceleration due to gravity)<sup>1</sup>.

The Sandia integrated surface micromachining process was selected for fabrication of the sensor due to the extreme measurement sensitivity potential associated with integrated microelectronics. Very fine measurement sensitivity was required due to the very small accelerometer proof mass ( $< 200 \times 10^{-9}$  gram) obtainable with this surface micromachining process. The small proof mass corresponded to small sensor deflections which required very sensitive electronics to enable accurate acceleration measurement over a range of 1,000 to 50,000 times the acceleration due to gravity. Several prototype sensors, based on a suspended plate mass configuration, were developed and the details of the design, modeling, fabrication and validation of the device will be presented in this paper. The device was analyzed using both conventional lumped parameter modeling techniques and finite element analysis tools.

The device was tested and performed well over its design range (the device was tested over a range of a few thousand G to 46,000 G, where 1 G equals the acceleration due to gravity).

### **Acknowledgements**

The authors wish to the outstanding fabrication and engineering analysis contributions by the entire Microelectronics Development Laboratory (MDL) staff.



## Contents

2.0	Introduction	6
3.0	Integrated Suspended Mass High-G Accelerometer Design	6
3.1	High-G Accelerometer Specification	7
3.2	High-G Accelerometer Mechanical Design (1 <sup>st</sup> Prototype)	7
3.3	High-G Accelerometer Electronic Design (1 <sup>st</sup> Prototype)	9
3.4	High-G Accelerometer Test Results (1 <sup>st</sup> Prototype)	9
4.0	Revised High-G Accelerometer Design	10
4.1	Finite Element Analysis of Revised High-G Design	11
4.2	Revised High-G Sensor Electronic Design	12
4.3	Testing Methods for the Revised Accelerometer Design	12
4.3.1	Revised Accelerometer Testing Overview	13
4.3.2	Revised Design Test Procedures – Laboratory Testing	15
4.3.3	Revised Design Test Procedures – Shock Lab Testing	16
4.4	Revised Accelerometer Design Test Results	16
5.0	Summary	18
6.0	Future Development	19
6.1	Microelectronics and Testing Electronics	19
6.2	Mechanical Electrostatic Damping	19
6.3	Packaging	19
6.4	Earth-Penetrator System Testing	19
	References	19
	Appendix	21

## Figures

Figure 1:	First Prototype Suspended Mass Sensor	7
Figure 2:	Schematic Mechanical Model	8
Figure 3:	Filtered Accelerometer vs. Time Plot for Shock Test at 10 kG	10
Figure 4:	Bent Beam Design for High-G Accelerometer	11
Figure 5:	Deflection Analysis of Revised High-G Accelerometer at 50 kG	12
Figure 6:	Block Diagram of Test Setup (1 <sup>st</sup> Prototype)	13
Figure 7:	Block Diagram of Revised Design Electronics	14
Figure 8:	Block Diagram of Test Setup (Revised Design)	15
Figure 9:	SEM Photograph of Fabricated Revised Accelerometer Design	17
Figure 10:	Filtered Acceleration vs. Time Plot for Shock Test at 25 kG	17
	Appendix Figures	25

## Tables

Table 1:	Finite Element Analysis Results (at 50 kG)	11
----------	--	----

# High-G Accelerometer for Earth-Penetrator Weapons Applications LDRD Final Report

## 2.0 Introduction

The acceleration environment experienced by the sensors and electronics in an earth-penetrator weapon is extreme, with average accelerations in the 20,000-G range and peak transient accelerations up to several hundred thousand G's. Earth penetrators often contact earth, concrete, rocks, or other hard materials while traveling at thousands of feet per second. Sensors must be able to survive both penetrator launch as well as contact and penetration while in some cases distinguishing between each. Commercially available accelerometers used in shock testing of earth-penetrator weapons components are both expensive (\$1800 each) and prone to failure.

The only reported silicon-based high-G accelerometers are bulk-micromachined. Preliminary failure analysis of these commercial sensors indicated that failure modes included both undamped high-frequency resonances of the sensor itself and catastrophic failure of the packaging<sup>2</sup> (included in the Appendix).

## 3.0 Integrated Suspended Mass High-G Accelerometer Design

A suspended mass, high-G accelerometer was designed and fabricated in a variation of Sandia's integrated surface-micromachined polysilicon / electronics manufacturing process<sup>3</sup>. This sensor consists of a parallel-plate capacitor, with one plate stationary with respect to the sensor housing and the second plate suspended by flexible beams that deflect in proportion to the magnitude of the acceleration imposed upon the sensor housing. The sensor was designed to measure accelerations up to 50 kG with a resolution of 50 G. Dominant design tradeoffs include balancing the requirement for plate deflections sufficient to obtain acceptable signal-to-noise ratios from the capacitive sensors against stiff mass suspension elements necessary to obtain responsive sensor measurements (high bandwidth). Additional design tradeoffs include optimizing response by designing a critically damped system subject to processing constraints. This design takes advantage of Sandia's new integrated surface-micromachining/CMOS manufacturing process to incorporate the capacitive pick-off electronics on-chip. Additionally, multiple sensors were fabricated together on the same chip, so that multiple sensors could be tested with a single shock, and the sensors could be readily used in a redundant, fault-tolerant architecture.

The mechanical elements of the high-G accelerometer were fabricated using two layers of polycrystalline silicon with a separation of two microns. The upper layer contains the moving mechanical element of the sensor, and the bottom layer acts as both a structural and electrical ground. The sensor principle of operation is to measure capacitance changes between the two plates with CMOS electronics located adjacent to the mechanical elements (same substrate).

### 3.1 High-G Accelerometer Specification

Nominal parallel-plate capacitance for the 50 kG sensor is 100 fF at a 2  $\mu\text{m}$  gap. This capacitance level is constrained by the necessity to interface with an existing CMOS microelectronics design. When no acceleration was applied to the sensor, its nominal capacitance requirement constrained both the gap spacing and plate overlap area. This translated into a plate overlap area of  $\approx 22,500 \mu\text{m}^2$  ( $\approx 150 \mu\text{m} \times 150 \mu\text{m}$  square area), where the no acceleration gap spacing was constrained by the 2  $\mu\text{m}$  thick sacrificial oxide layer used in the fabrication process. The desired gap spacing during acceleration of 50 kG is 1  $\mu\text{m}$ . The resonant frequency of the sensor suspension is constrained to be greater than 100 kHz to accommodate sampling frequencies and the induced vibration caused by the sampling voltage electrostatic attractive force. To obtain adequate response, a target range of 0.4 to 0.6 for the damping ratio is desired. This range was principally dictated by fabrication considerations, specifically the requirement for sufficient spacing of etch-release holes. In this case, there is very little design flexibility to control damping using the mechanism of squeeze-film damping of the air surrounding the sensor

### 3.2 High-G Accelerometer Mechanical Design (1<sup>st</sup> Prototype)

The first prototype suspended mass sensor consists of fourteen beam elements (seven on each side) that act as springs to cantilever a  $22,600 \mu\text{m}^2$  plate mass (top layer of polycrystalline silicon) over a bottom electrode (bottom layer of polycrystalline silicon). A top view of the sensor and reference capacitor is shown in Figure 1. The sensor consists of two plate masses, one of which serves as a reference capacitor during acceleration measurements. The sensor element on the right is suspended by 14 beams, each 7  $\mu\text{m} \times 90 \mu\text{m}$  in size. Each beam acts as a spring allowing the square plate mass in the center of the sensor to move up or down. The reference capacitor, on the left, is a parallel plate capacitor identical in geometry to the sensor parallel plate capacitor with the exception of spring elements. Spring elements in the reference capacitor are designed to be very stiff, so that at the acceleration levels relevant to sensor operation, the spring elements permit negligible deflection of the plate mass. The reference capacitance and sensor capacitance are compared electronically to measure acceleration.

Each suspended mass is perforated by 324, 2 $\mu\text{m} \times 2\mu\text{m}$  etch-release holes. The number and spacing of the etch-release holes (necessary for proper fabrication of the sensor element) results in a damping ratio at 50 kG of acceleration of  $\approx 0.4$ . The calculated natural frequency of the sensor is  $\approx 127 \text{ kHz}$  with a damped natural frequency of  $\approx 118 \text{ kHz}$ . Cross-axis sensitivity should be minimal and the fracture factor of safety of the device was calculated to be almost three. Results of testing the suspended mass prototype sensor are included in sections 3.4 and 4.4 of this paper.

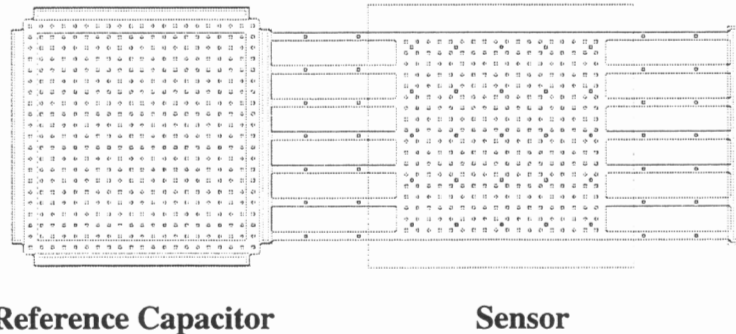


Figure 1: First Prototype Suspended Mass Sensor

Damping was determined by simultaneously applying three different models of squeeze film damping, each of which models some but not all of the applicable characteristics of the suspended mass prototype. Squeeze-film damping can be defined as the viscous loss of energy due to pumping a viscous fluid out from or into the volume between two moving surfaces.

The first model<sup>4</sup> is applicable to squeeze-film damping between two parallel disks without perforations that are separated by several microns. In this model, viscous damping occurs due to the movement of fluid around the outside edges of the plates. The damping resistance,  $R_{\text{film}}$ , is characterized by the following equation:

$$R_{\text{film}} = 3\mu S^2/2\pi\delta^3 \quad (\text{N-s/m}) \quad (1)$$

where  $\mu$  is the fluid viscosity ( $18 \times 10^{-6}$  kg/m-s for air at 20 °C),  $S$  the plate area overlap, and  $\delta$  the average plate spacing.

The second model<sup>4</sup> is applicable to squeeze-film damping when one plate is perforated. In this model, viscous damping occurs due to the flow of fluid through the perforations. The damping resistance,  $R_{\text{perf}}$ , is characterized by the following equation:

$$R_{\text{perf}} = 12\mu S^2/N\pi\delta^3 G(A) \quad (\text{N-s/m}) \quad (2)$$

where  $A$  is the fraction of open area in the plate, and  $N$  is the total number of holes in the perforated plate. The function  $G(A)$  is described in equation (3).

$$G(A) = [A/2 - A^2/8 - (\ln A)/4 - 3/8] \quad (3)$$

The third model<sup>4</sup> is applicable to squeeze-film damping at high frequencies ( $> 10$  kHz). This viscous resistance is called radiation resistance and is characterized by the following equation:

$$R_{\text{rad}} = \rho c (A\omega/c)^2 \quad (\text{N-s/m}) \quad (4)$$

where  $\rho$  and  $c$  are the density and speed of sound of the viscous fluid, and  $\omega$  is the frequency of motion. Each of the three models was applied to the design of the suspended mass accelerometer by modeling each of their respective damping contributions and combining them as parallel elements (as shown in Figure 2).

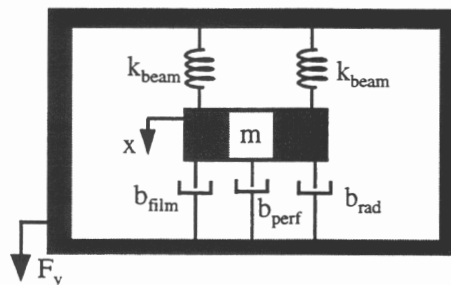


Figure 2: Schematic Mechanical Model

### 3.3. High-G Accelerometer Electronic Design (1<sup>st</sup> Prototype)

The CMOS circuit for the high-G accelerometer consists of a unity gain buffer followed by a gain stage and output driver. The purpose of the circuit is to measure the change in capacitance of the sensor capacitor relative to the fixed reference capacitor. The sensor capacitor and the reference capacitor are connected in series and an AC signal (100 kHz,  $\pm 5$  V P-P) is applied across the pair. If the two capacitors are not equal, an output signal appears at the common node of the pair. This signal is proportional to the acceleration and is sensed by the CMOS circuit.

Since the sensor capacitors are small, the input capacitance of the circuit is also very small. The first stage consists of an n-channel source follower with an input capacitance of  $\cong 40$  fF. Noise limits the sensitivity of the circuit, so the circuit was designed to have an input noise of less than  $2\mu\text{V}/\text{Hz}^{1/2}$ . The second stage is a combination gain stage and output driver. The gain is  $\cong 100$  and the output driver is designed to be compatible with the off-chip loads.

Integrating the CMOS electronics on the same substrate as the micromachines enables the microelectronics to measure extremely small capacitance changes (on the order of fractions of atto Farads). This enables the sensor to be operated over a high dynamic range and still measure relatively small changes in acceleration. Additionally, parasitic noise is reduced while bandwidth is increased in the integrated electronics configuration.

### 3.4 High-G Accelerometer Test Results (1<sup>st</sup> Prototype)

Preliminary test results for the first suspended mass accelerometer prototype demonstrated reasonable correlation between acceleration levels and sensor output at G levels under 15 kG (6 kG, 10 kG, and 14 kG). At higher G levels (above 16 kG), sensor output was saturated and so could not be accurately correlated to acceleration level.

The suspended mass accelerometer output signals also appeared to contain carrier signal components, shock signal artifacts, and unidirectional output bias. A filtered sample test trace is included in Figure 3. A number of electronic as well as mechanical issues that likely contributed to the sensors' operation were identified and addressed. These issues included residual stress in the suspended mass suspension, resonant overtravel, output bias, underdamped mass motion, output amplifier saturation, excessive design gain, and incomplete comparator signal cancellation.

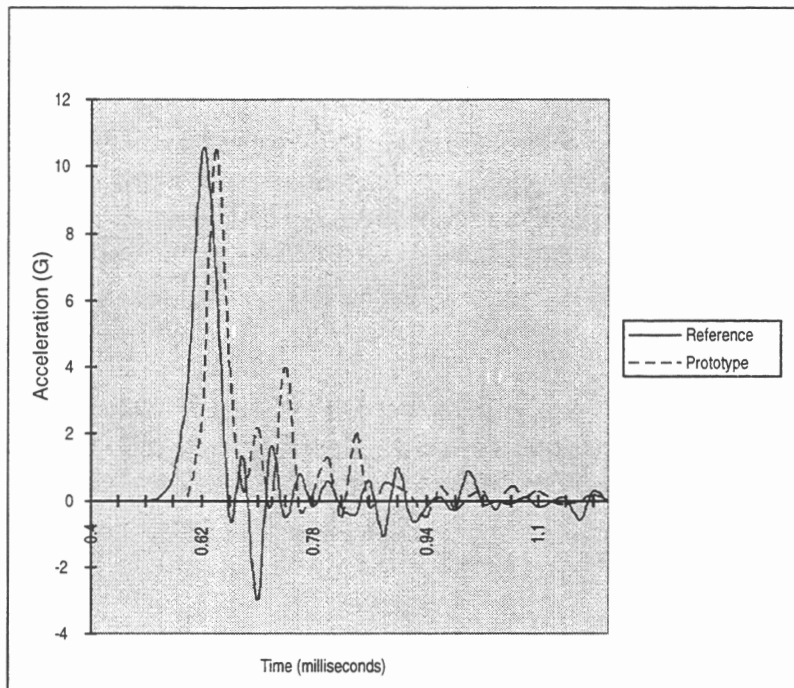


Figure 3: Filtered Acceleration vs. Time Plot for Shock Test at 10 kG

#### 4.0 Revised High-G Accelerometer Design

Two different revised mechanical designs were developed and are currently being fabricated using the Sandia integrated process. The first revised mechanical design is shown in Figure 4. In this design, the suspension system was modified to incorporate greater compliance in both the vertical and horizontal directions. The additional vertical compliance was added to enable increased movement of the plate mass in the sensing direction. The additional horizontal compliance was added to relieve any residual stress that might remain in the structural polycrystalline silicon after processing. The bent beams provide stress relief in the horizontal plane. Both the mechanical design and CMOS circuit design used in the first suspended mass prototype were enhanced to resolve performance reduction factors identified in the previous section. The revised mechanical element was designed to be compatible with the improved CMOS circuitry.

An additional mechanical design was developed to be compatible with a new CMOS sensing circuit. Both the electronic circuitry and the mechanical design were based on an inertial sensor designed at the University of California at Berkeley and fabricated at Sandia<sup>5</sup>. Both the electronic and mechanical elements of the Berkeley design were adapted to the high-G acceleration environment. CMOS circuitry compatibility required the use of a sensing mass with a much larger capacitive area ( $72,900 \mu\text{m}^2$  with a nominal capacitance of 325 fF) than was used in the previous accelerometer design.

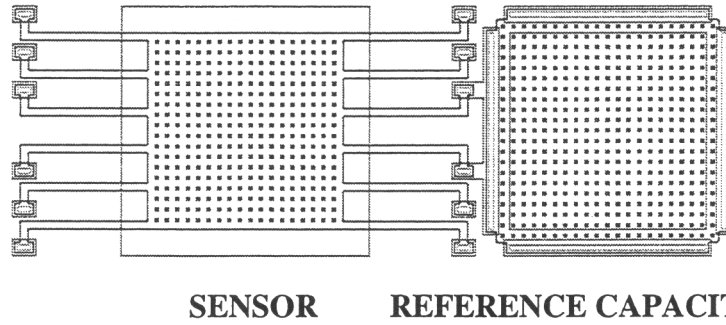


Figure 4: Bent Beam Design for High-G Accelerometer

#### 4.1 Finite Element Analysis of Revised High-G Design

Finite element analysis software was used to verify the design of the bent beam high-G accelerometer. The finite element software that was used is called ANSYS/AutoFEA<sup>®</sup> 3D, and is compatible with AutoCAD<sup>®</sup> generated geometry. Results of this analysis software predicted somewhat different deflection and resonant frequency values than those obtained through manual analysis. The software predicted that the structure would resonate at 151 kHz (Table 1) as compared to the manual analysis prediction of 101 kHz. The finite element software predicted maximum deflection at 50 kG of 0.64 microns (Figure 5) compared to 0.95 microns using manual analysis techniques. Additionally, finite element software predicted a maximum principal stress level of 93.2 MPa (Table 1) at 50 kG compared to 74 MPa using manual analysis techniques.

<ul style="list-style-type: none"> <li>• Vibration Frequencies: <ul style="list-style-type: none"> <li>– Mode 1: 151 kHz</li> <li>– Mode 2: 240 kHz</li> <li>– Mode 3: 470 kHz</li> <li>– Mode 4: 498 kHz</li> <li>– Mode 5: 747 kHz</li> <li>– Mode 6: 876 kHz</li> </ul> </li> </ul>	<ul style="list-style-type: none"> <li>• Maximum Deflection (@ 50 k-g's): <ul style="list-style-type: none"> <li>– 0.64 microns</li> </ul> </li> <li>• Maximum Stress (@ 50 k-g's): <ul style="list-style-type: none"> <li>– 93.2 MPa</li> </ul> </li> </ul>
--	--

Table 1: Finite Element Analysis Results (at 50 kG)



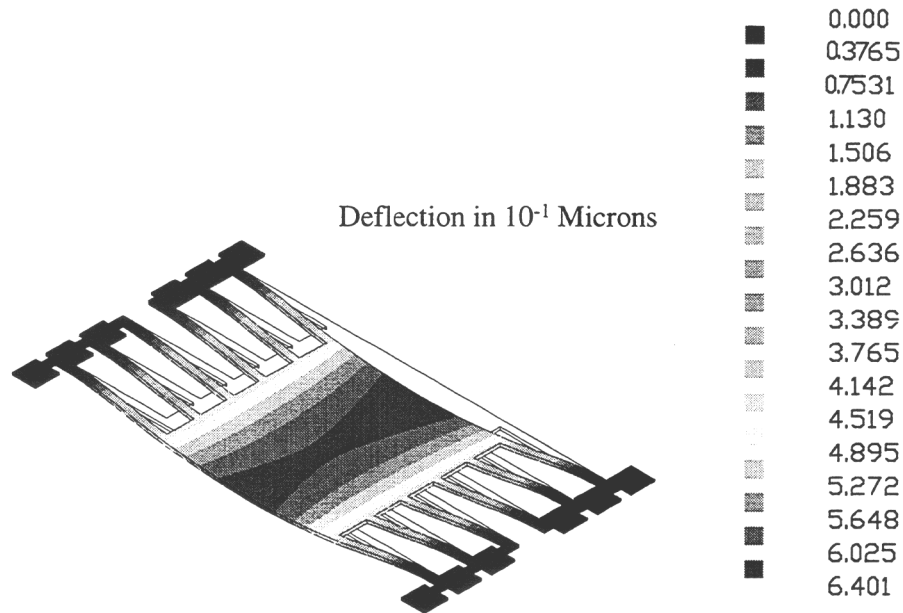


Figure 5: Deflection Analysis of Revised High-G Accelerometer at 50 kG

#### 4.2 Revised High-G Sensor Electronic Design

The CMOS circuit for the revised high-g accelerometer consists of a unity gain buffer followed by a multiplier and low-pass filter. The purpose of the circuit is to measure the change in capacitance of the sensor capacitor relative to the fixed reference capacitor. The sensor capacitor and the reference capacitor are connected in series and an AC signal is applied across the pair. As in the case of the first prototype electronic design, if the two capacitors are not equal, an output signal appears at the common node of the pair. This signal is proportional to the acceleration and is sensed by the CMOS circuit.

The multiplier stage is used to demodulate the signal from the buffer. The buffer output is multiplied by the AC signal that was applied to the sensor. In effect the output of the buffer is an AM signal. The AC input signal applied to the sensor is the carrier and the acceleration is the data. The input differential amplifiers use source followers as loads to predistort the data to maximize the linearity of the multiplier.

The low-pass filter is a second order active filter. The cutoff frequency of the filter is 100 kHz. This Butterworth filter is designed to eliminate any switching noise from the multiplier. The output stage of the op amp is designed to drive loads down to 1 k $\Omega$ . When a 100 kG acceleration is applied to the device the sensor capacitor should increase from 100 fF to 200 fF. For this acceleration, the amplitude of the waveform at the output of the filter will be 2 V. The gain of the CMOS circuit can be varied by changing the amplitude of the AC signal applied to the sensor.

#### 4.3 Testing Methods for the Revised Accelerometer Design

Figure 6 is a simplified view of the accelerometer sensor at rest. One of the capacitors shown has the plates fixed (reference or fixed capacitor) while the other capacitor has one plate which at rest is floating

(sensor) and can move when exposed to acceleration. The two capacitors are connected in series and form a capacitive divider. The two inputs into the device are driven differentially by a 1 MHz square wave. Ideally, the value of the capacitors are equal at rest and the amplitudes of the square waves on each capacitor are equal but  $180^\circ$  out of phase. With no acceleration, the two signals cancel at the common summing node and the voltage to the amplifier is zero. When acceleration is detected the floating plate moves and changes the value of the sensor capacitor producing a voltage at the summing node proportional to the amount of deflection. Information on the direction of the acceleration is contained in the phase of the signal that is produced.

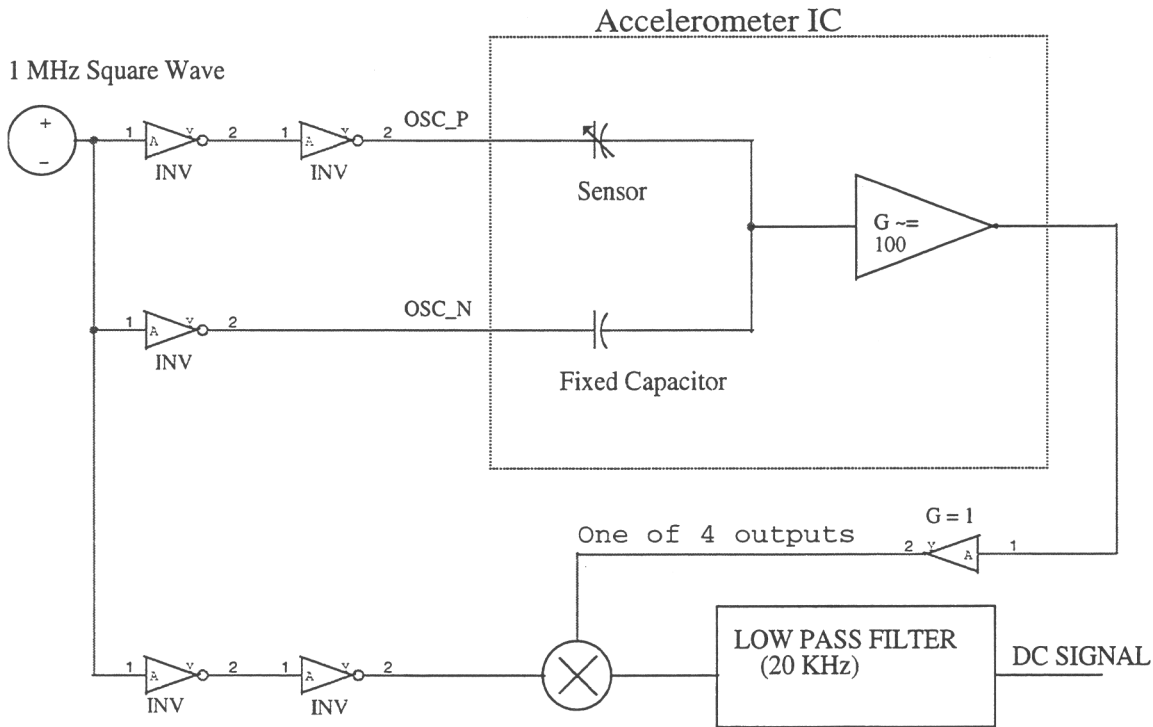


Figure 6: Block Diagram of Test Setup (1<sup>st</sup> Prototype)

The signal produced at the amplifier's input is amplified and fed to a multiplier circuit which multiplies this signal with an in-phase copy of the original square wave. If the sensor produced signal is in phase with the square wave a positive voltage will result. If the sensor signal is  $180^\circ$  out of phase with the square wave a negative voltage will result. This multiplier output is then filtered to remove spurs resulting in a voltage proportional to the acceleration sensed.

#### 4.3.1 Revised Accelerometer Testing Overview

Two iterations of devices were tested. The first device included four copies of the capacitive sensor each followed by an internal amplifier as shown on Figure 6. All remaining circuits were external to the device. The second iteration device included four sensors each with different electronic circuits. One of the four circuits on the second device was the same as for the original devices. The other three circuits had differences in the electronics such as amplifier gain and amount of additional electronics shown external to the device. On one of the circuits, except for an internal oscillator, all the functionality

needed to perform an acceleration measurement was integrated into the device. Figure 7 is a block diagram of the second design iteration accelerometer IC.

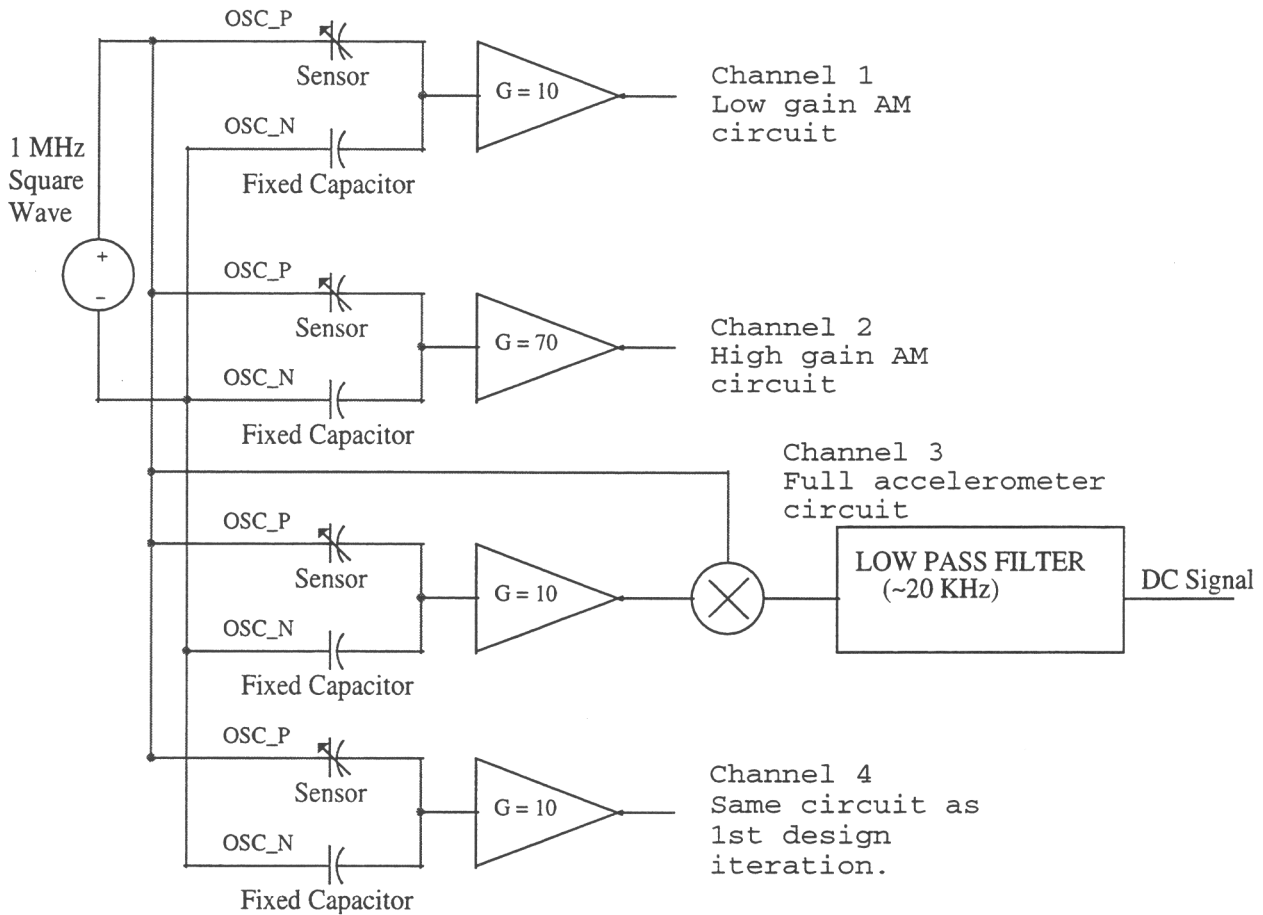


Figure 7: Block Diagram of Revised Design Electronics

For each design iteration the devices were initially evaluated in the lab to determine the electronic operating points, such as, power consumption, frequency response, and amplifier gain. A test box designed and assembled by Sandia's Intelligent Micromachine Department was received along with the initial test devices. To interface the test box to the device under test, wires were soldered directly to the pins of the device. A test fixture was fabricated to mount the device and the test box was attached to the fixture with foam to allow the box to ride along with the device.

Initially the shock table operated by Sandia's Manufacturing and Rapid Prototyping (Shock Testing) Department was used to test the devices. The shock table has the capability to provide shock levels up to approximately 10,000 g's. During the shock table testing, outputs from the device which correlated to outputs from an Endevco accelerometer were not detected. The test box also proved to be problematic because it had not been designed and fabricated to withstand high level mechanical shock. A new test box was designed and fabricated and potted in water soluble wax to withstand the environment. The accelerometer test system showing the new test box design is given in Figure 8. The accelerometer IC was also potted with wax in the shock fixture. Again outputs could not be detected using the shock table.

A decision was made to move the testing to the Hopkinson bar<sup>6</sup> shock facility, also operated by Sandia's Manufacturing and Rapid Prototyping (Shock Testing) Department, which could provide much higher levels than the shock table.

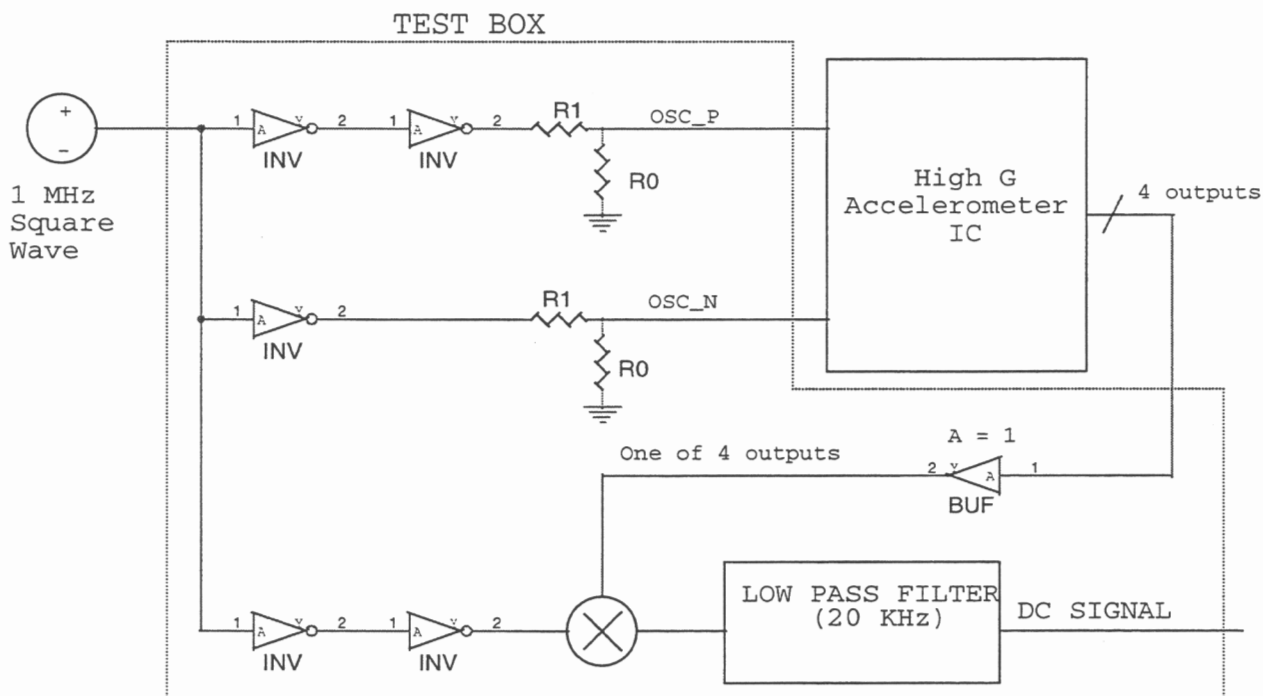


Figure 8: Block Diagram of Test Setup (Revised Design)

A new test fixture was fabricated to mount the accelerometer IC to the Hopkinson bar. Initial testing on the Hopkinson bar again was inconclusive. Since wiring directly to the IC pins is very burdensome and necessary each time a new device is to be shock tested we decided to fabricate PC boards to mount the devices. Additionally, IC outputs were directly monitored to eliminate the test box as the failure mechanism. This final test configuration was used to complete shock lab testing on the first prototype accelerometers and was also used for final shock testing of the revised accelerometer devices.

#### 4.3.2 Revised Design Test Procedures – Laboratory Testing

This testing was performed on all devices received on a laboratory protoboard.

1. Power consumption with inputs grounded apply plus 5 volts and minus 3 volts to the positive and negative supply pins with an ammeter in series and record the current drawn from each supply.
2. Input and output continuity checks and amplifier response
  - a. Apply a 1 volt peak square wave signal to the OSC\_P input and signal ground to OSC\_N input. Beginning with 1 kHz change the square wave frequency to 10 kHz, 100 kHz, and 1 MHz. Record the output wave form peak-to-peak amplitude and DC offset voltage for all four outputs at each frequency.
  - b. Repeat a except ground the OSC\_P input and apply the signal to the OSC\_N input.
  - c. Repeat a except apply the signal to both the OSC\_P input and the OSC\_N input.

- d. Repeat a, b, and c, except change input signal level to 2.5 volts peak.
3. Determine output cutoff frequency  
Apply inputs as in 2 c above and adjust the input amplitude and frequency to get a good output signal at least 1 volt peak-to-peak. Vary the frequency of the input signal until the output falls to one-half the original output. Record the high and low frequencies where this occurs.

#### **4.3.3 Revised Design Test Procedures – Shock Lab Testing**

Based on the results of the laboratory testing, a device is selected and mounted for shock testing. The shock lab operator will need access to the device outputs for monitoring. These outputs can be accessed with the use of a 15 pin MDM break out box connected to the cable that also provides power and input signals.

Prior to performing the shock test, measure power supply voltages to assure correct values of plus 5 volts and minus 3 volts. Monitor the input signals to assure the signals are 2.5 volts peak and 180° out of phase.

#### **4.4 Revised Accelerometer Design Test Results**

The first iteration devices were checked in the lab and found to have the amplifier quiescent point sitting near the negative power supply rail of -3 volts. This effectively clipped the negative portion of the AC signal. Extensive lab testing to check if power supply voltages other than +5 and -3 volts would move the quiescent point closer to zero volts was not successful. In addition, internal amplifier compensation created an amplifier response cutoff frequency of approximately 165 kHz. Because of the amplifier frequency response, the input frequency was changed to 100 kHz for the first accelerometer IC design iteration.

Initial tests using the shock table were inconclusive. Some variables in the testing were due to the test setup, especially the test box, and not just the device under test. In addition, the sensitivity of the devices to the shock was unknown. The shock table had a maximum shock capability of about 10,000 G while higher levels were desired. The change to the Hopkinson bar allowed for higher shock levels but initially was still inconclusive. To remove variables in the testing due to the test box the accelerometer IC outputs were monitored directly while tweaking the power supply voltages.

The expected outputs from the accelerometer IC without the test box were amplitude modulated (AM) copies of the input waveforms with an envelop resembling the applied shock pulse. A wooden mallet was used to tap the shock fixture while the outputs were monitored along with the reference Endevco accelerometer. During this checkout, one half of the expected AM output signal was detected. The negative excursion of the AM signal was clipped as expected. This observation indicated that the capacitive sensor element in the IC was functioning and failure to observe a shock pulse was due to the internal amplifier and/or external test circuitry. This device response was recreated on the Hopkinson bar by monitoring the outputs directly. All subsequent testing was performed in this fashion.

As mentioned earlier and given in Figure 7, the accelerometer IC was redesigned to integrate more of the test circuitry in the device. When the new devices were delivered and initially lab tested they were found to be oscillating. This may have been due to a reduction in the amplifier compensation. The amount of compensation was reduced to get a higher frequency response from the internal amplifiers. With no output loads, channels 1 and 2 were found to be oscillating at approximately 3.1 MHz with amplitudes as high as 6 volts peak-to-peak. In an effort to reduce the oscillation, bypass capacitors were added to the power supply inputs and 1 k $\Omega$  resistors were added to the outputs. Although the oscillation was not removed it was reduced in amplitude to approximately 100 millivolts peak-to-peak for channels 1 and 2. The oscillation frequency also changed to approximately 2.3 MHz. Channels 3 and 4 also had oscillations but the levels were much lower, about 30 millivolts peak-to-peak, due to the internal filter on channel 3 and low frequency response of the internal amplifier on channel 4. Although the oscillation could not be removed, the reduction in amplitude was enough to continue the evaluation at the shock facility. The oscillation noise could be filtered with post processing of the data.

A number of new failure modes were discovered once shock testing reached levels of 25,000 G and above. For instance, at 25,000 G, die adhesive failure was experienced that caused the chip to separate from the package during shock testing. This was traced to a chemical incompatibility introduced during the final etch release process. At approximately 40,000 G, the packages began to crack. This was corrected by modifying the lid seam sealing operation to reduce the mechanical stress concentrations coincident with the lid edges and modifying the mounting bracket to better distribute the mechanical stresses imposed by the bracket against the package during shock testing. These modifications corrected both the die adhesion and package cracking failures previously experienced.

Figure 9 below shows a Scanning Electron Microscope (SEM) photograph of the fabricated revised suspended plate mass accelerometer with associated microelectronics and reference capacitor. The fabrication process took approximately three months and required hundreds of correctly and precisely completed process steps.

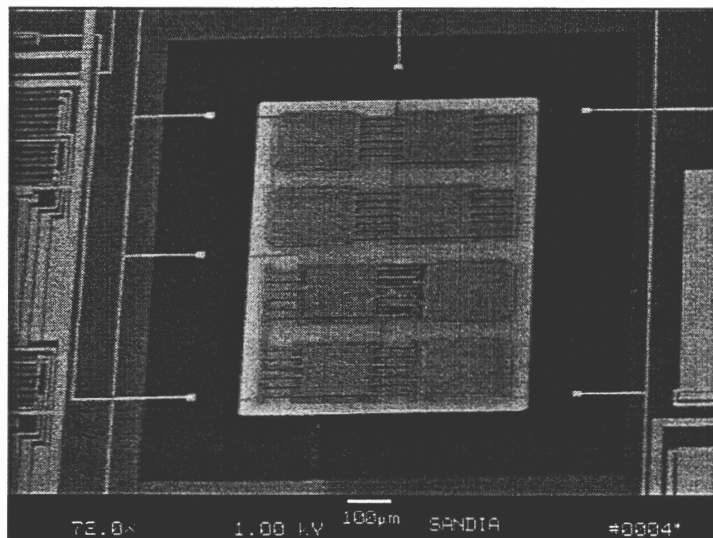


Figure 9: SEM Photograph of Fabricated Revised Accelerometer Design

Test results for the revised Sandia designed accelerometer were very positive, with the response of the sensor showing excellent correlation between the shock pulse and sensor output at accelerations up to 50,000 G (actually tested at 46,000 G). Filtered accelerometer response data is shown for a shock pulse of approximately 25 kG in Figure 10 below.

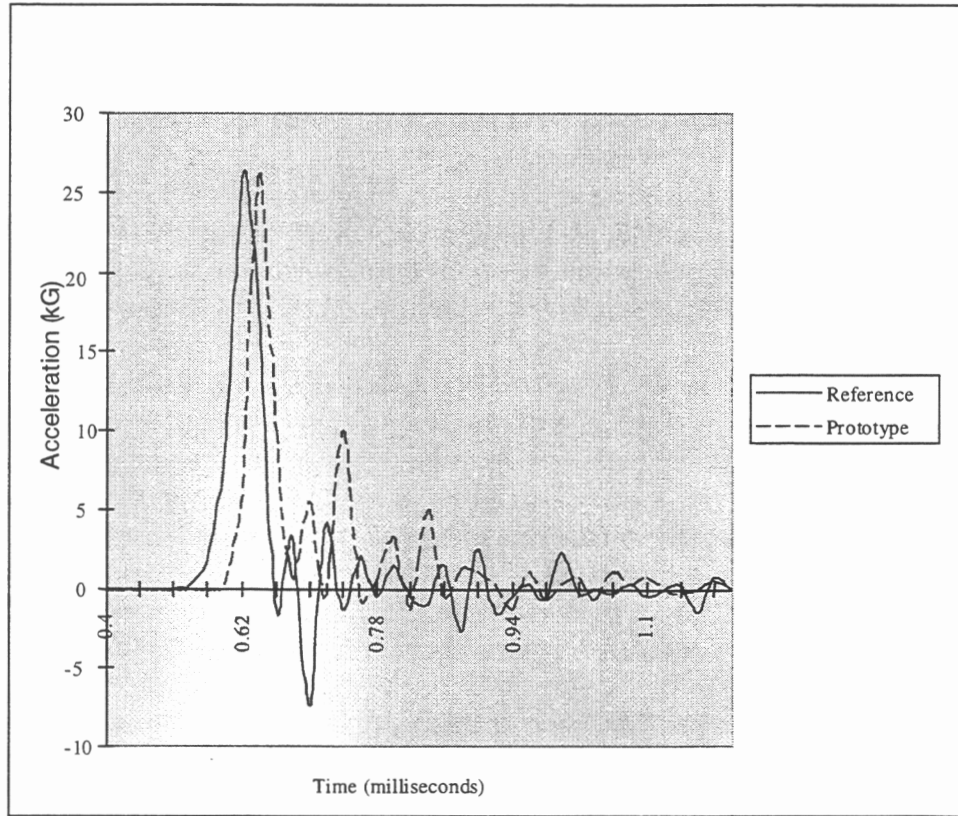


Figure 10: Filtered Acceleration vs. Time plot for Shock Test at 25 kG

## 5.0 Summary

The mechanical sensor element, supporting microelectronics, and packaging have been proven to operate properly at acceleration levels up to 46,000 G. The first prototype suspended mass high-G accelerometer design showed promising results up to 14 kG, but was not suitable for higher acceleration levels. A second generation series of designs have been developed to improve and correct those factors that contributed to the unsatisfactory performance of the first prototype. These second generation prototypes include two different mechanical designs and three different electronic circuit designs. The second generation prototypes were successfully tested up to 46,000 G, with various modifications in the testing and packaging processes necessary to eliminate failures due to die adhesion and package cracking.



## **6.0 Future Developments**

### **6.1 Microelectronics and Testing Electronics**

The internal electronics need to be redesigned and characterized to allow calibration of the sensors and improvements in the quality of the sensor output signal. Microelectronics design of next generation devices should incorporate the support electronics that have been externally connected to previous generation devices during testing. Additional signal processing and integration electronics also need to be developed and tested to both simplify future integration and improve sensor output.

### **6.2 Mechanical Electrostatic Damping**

Sensor response and reliability might be greatly improved with the addition of controlled mechanical damping. Controlled damping is necessary to maintain optimal damping ratio in order to minimize proof mass vibration amplitude and duration. Vibration results in signal distortion and mechanical damage to the sensor element. Squeeze-film damping is essentially fixed once the sensor is fabricated and is significantly constrained by the number and spacing of etch release holes. The addition of electrostatic damping could be implemented to facilitate real-time control of the proof mass damping and thus improve the performance of the sensor. Electrostatic damping would consist of additional electrodes and electronics to provide both a mechanism for sensing relative velocity between the sensor proof mass and housing, and then applying an appropriate electrostatic damping force to control and attenuate sensor motion.

### **6.3 Packaging**

Ceramic packages proved to be a significant limitation at high shock levels. Plastic or stainless steel packaging might need to be substituted for ceramic packages, especially for future sensors that might be designed for accelerations exceeding 100,000 G. Other issues such as shock pulse distortion, packaging deformation, and the hermetic capabilities of the packaging configuration must also be addressed. Bond pad layout on the sensor chip must also be collaborated with the package pin layout to optimize bond wire length and configuration.

### **6.4 Earth-Penetrator System Testing**

The most important test for the accelerometer will be the integration and operation of the accelerometer chip in an earth-penetrator weapon test. This will require full integration of the device with the instrumentation of the earth-penetrator with many support electronics functions integrated within the accelerometer microelectronics. Electronic and mechanical interfaces will need to be defined and developed in order to complete this portion of the accelerometer testing.

## **References**

1. B. R. Davies, S. Montague, J. H. Smith, M. Lemkin, "Micromechanical Structures and Microelectronics for Acceleration Sensing", Proceedings of SPIE Micromachining and

- Microfabrication Conference, *Micromachining and Microfabrication Process Technology III*, Volume 3223, pp 237-244, Sept., 1997.
2. T. Christenson, "Failure Analysis of Endevco 7270A High G Accelerometer", Sandia Internal Report, 1997 (included in the Appendix).
  3. J. Smith, S. Montague, J. J. Sniegowski, J. R. Murray, and P. J. McWhorter, "Embedded Micromechanical Devices for the Monolithic Integration of MEMS with CMOS," *IEDM Tech. Digest*, pp. 609-612, Dec. 1995.
  4. T. B. Gabrielson, "Mechanical-Thermal Noise in Micromachined Acoustic and Vibration Sensors", *IEEE Transactions on Electron Devices*, Vol. 40, No. 5, May, 1993.
  5. M. A. Lemkin, M. A. Ortiz, N. Wongkomet, B. E. Boser, J. Smith, "A 3-Axis Surface Micromachined  $\Sigma\Delta$  Accelerometer", *IEEE International Solid-State Circuits Conference*, pp. 202-203, 1997.
  6. V. I. Bateman, R. G. Bell, and N. T. Davie, "Evaluation of Shock Isolation Techniques for a Piezoresistive Accelerometer", *Proceedings of the 60<sup>th</sup> Shock and Vibration Symposium*, Volume I, November 14-16, 1989.

## Appendix

### Failure Analysis of Endevco 7270A High G Accelerometer

Todd Christenson, 2643

#### Introduction

This report summarizes efforts to understand how failures occur in the Endevco 7270A line of high G accelerometers. An extensive history of failure during test has been cited for these accelerometers in which the supposed mode of failure was the excitation of high frequency resonant modes leading to some mechanical failure. This line of reasoning was supported by the fact that 200kG accelerometers failed after receiving only 10kG shocks [ 1 ]. Such behavior has motivated an attempt to identify the particular failure mechanism so that it may be avoided in future micromachined sensor development.

#### Testing

Three types of testing were pursued in sequence starting with optical microscopy and SEM examination followed by electrical testing and finally acoustic microscopy. In order to reveal the accelerometer die, a method to gently remove the cover was needed. The package was clamped to the base of an end mill and the cover weld was @lled off with several thin passes until the cover became loose at which point it could be popped off with a tweezer. The layout of the die with respect to the package as well as the wiring configuration is shown in the photographs of Fig. 1. The die itself measures 1 mm x 1 mm and is nominally 200 micrometers thick. The bond wire is 2 niil in diameter and is potted at the header and die bond areas. Double sided wafer processing is used to fabricate a fully active bridge circuit consisting of two resistors on each side (top and bottom) of the die. The entire die is attached to an intermediate layer of silicon (the "pedestal") which has etched grooves to accommodate proof mass movement as well as wire bonding to the underside of the die. The die is bonded to the pedestal with a low melting temperature glass (500 °C) [2].

A drawing of the sensor is provided from ref. [3] and is depicted in Fig. 2. The die consists of two cantilevered masses defined by double sided anisotropic etching of (I 10) oriented silicon resulting in an I-beam shaped structure. The sensing takes place in piezoresistive gages which are strung across the high stress region of the cavity of the formed i-beam and are fabricated by a p+ diffusion on the top and bottom surfaces of the silicon die. These doped regions are subsequently resistant to the anisotropic etching step which defines the accelerometer mass. The dimensions of the cantilevered mass and gages are shown in Fig. 3.

Devices were initially inspected using optical and scanning electron microscopy. A total of 10 devices were examined 5 of which were good and 5 of which failed. One failed and one good device was destroyed while machining off the covers. Figure 4 shows an optical micrograph of a good device. Two of the failed devices, both returned from Eglin AFB, had obvious mechanical failure. As shown in Fig. 5 one device had a chipped proof mass and the other had both proof masses entirely separated from the main body of the sensor. The other failed devices had no visible defects and thus electrical tests were subsequently performed.

The die bonding and header metallization is configured to achieve a bridge connection as shown in Fig. 6. Electrical connection is made to the bridge by applying an excitation between the black and read leads

and measuring output between green and white. Electrical measurements were made by probing each individual resistor gage (8 per resistor arm). Only the top die resistors were measured. Probing the bottom resistors would require melting the glass bond to the pedestal for which there has yet to be motivation. An example of such a measurement for a good device is shown in Fig. 7 for the die depicted in Fig. 8. The resistor map shown in Fig. 7 is typical of the resistance distribution across a resistor arm. The measurement was made in circuit and thus is in parallel with the remainder of the bridge. The bridge is balanced by breaking parallel resistor bridge paths on the main die body. The resulting resistance increase introduced in the resistor arm can also be measured and is seen in Fig. 7. Although the difference in each resistor arm can be as great as 100 ohms the input resistance tracks output resistance to better than the measurement accuracy 2 ohms). For the device in Fig. 7 the input and output resistances were 654 and 656 ohms respectively which is within the specified range of 550-+200 ohms.

Resistor maps of two failed devices are shown in Figs. 9 and 11 for the corresponding die photos in Figs. 10 and 12. The device in Fig. 9 showed no electrical problems. The device in Fig. 11 measured high resistance values (10k $\Omega$  range) between green-black and white-red which are attached to the two top die resistor arms. The same resistance levels were measured before opening the package as well. Upon measuring the die itself, however, all resistors were intact as shown in Fig. 11. Problems with bonding was subsequently suspected and found in the wire itself. While probing the bond wire leading to the top resistors a break in the bond wire itself was found with the wires being held in place by a small amount of potting material. After probing the wires they became completely separated as shown in Fig. 13. A summary of measurements is listed in Table 1. It should also be noted that for the device with the chipped proof mass shown in Fig. 5, the remaining piezoresistive bridges along that resistor arm remained electrically intact.

Resistance	<u>Device</u>		
	III (Fig.8)	H (Fig. 10)	A2 (Fig. 12)
R-G	475	531	733
G-B	462	498	open (725 on die)
B-W	506	532	603
W-R	518	565	open (625 on die)
R-B (Rin)	654	702	open
G-W (Rout)	656	706	open
outcome	good device	no electrical problem	broken bonding wire

Table 1. Measurement summary. All resistance values in ohms.

In order to identify additional mechanical failures in failed devices for which no electrical problems could be found, acoustic microscopy was used [5]. Such testing can reveal cracks which can not be observed optically. Example images are shown in Fig. 14. The various colors indicate variation in acoustic impedance. Thus, anomalies in the color pattern indicate regions of structural changes. In particular, the piezoresistor bridges were examined for cracks. Nothing conclusive was found, however, and all anomalies with respect to the accelerometer die were attributed to particles which either came from the package or the liquid used in the acoustic measurement.

## Results

The measurements on the available failed devices point out several concerns. The dominant issue appears to be packaging difficulty which stems from the requirement to have a mechanical element in an electrical package which must be free to move thus precluding potting of the entire device. An additional problem results from the fact that single crystal silicon has a high quality factor (has been measured as high as 200,000) and thus can be a very efficient resonator.

The packaging difficulty lead to two major problems. Since there are open spaces within the package, debris may be dislodged and cause damage to the device under shock. An abundance of particles were seen upon opening all of the devices. In addition, the partial potting of the bond wires may be compounding the problem of bond wire failure. Although the potting was seen to vary substantially, the nominal profile is one where most of the potting compound resides beneath the bond wire with comparatively small thickness above the wire. Such a configuration may act to create a larger moment on the wire and thus magnify the tensile shock load along the bond wire.

There are three elements in the device which may potentially resonate. The bond wires as potted have free portions between the header and die which may be susceptible to resonating. This is very difficult to characterize, however, since the wire lengths vary greatly and do not have a well defined shape. Estimates for ranges of resonant frequencies are between 50 and 300 kHz. The wire resonance is likely to be highly damped, however, due to damped ends provided by the plastic potting material.

Although none of the bridge piezoresistors were found to fail, these beams are prone to resonance. Estimates for the resonant frequencies are 20 MHz, 57 MHz, and 110 MHz for the first, second, and third modes respectively. The frequencies were calculated assuming a clamped-clamped beam with rectangular cross section and a silicon Young's modulus of 190 GPa.

The obvious resonant mode of concern is with respect to the proof masses. Using the measured dimensions in Fig. 3 a numerical model was constructed and resonant mode calculations were done as shown in Figs. 15 [6]. The first three resonant frequencies are found to be 780 kHz, 5.8 MHz, and 7.0 MHz and fall within the range of concern for possible shock frequency components.

## Conclusions / Recommendations

The initial examination of the 7270A device has revealed a significant concern with packaging. A means to determine the optimal bonding technique would be to conduct shock tests on various bond configurations with an inactive die. The onset of lead separation may be detected in the existing device

by modeling the bridge with a series resistance in each of the four leads. Circuit analysis combined with external bridge resistance measurements will reveal discrepancies to the ideal bridge result even when the bridge appears balanced. A greater number of failed devices would be of help to identify problems in failed devices with no apparent physical damage.

## References

- [1] David E. Ryerson, Vesta I. Bateman, "High Shock Accelerometers," Sandia Internal Report, August 26, 1996.
- [2] Bruce Wilner, designer of Endevco 7270A, Endevco Corp., Sunnyvale, CA, private communication.
- [3] Robert D. Sill, "Testing Techniques Involved with the Development of High Shock Acceleration Sensors," Endevco Tech Paper TP284, Feb. 1984.
- [4] Endevco Corporation "Piezoresistive Accelerometer - Endevco Model 7270A" Data Sheet.
- [5] John Gieske, Sandia Acoustic Emissions Lab, private communication.
- [6] Ernest J. Garcia, Sandia Electromechanical Engineering, private communication.

## Figures

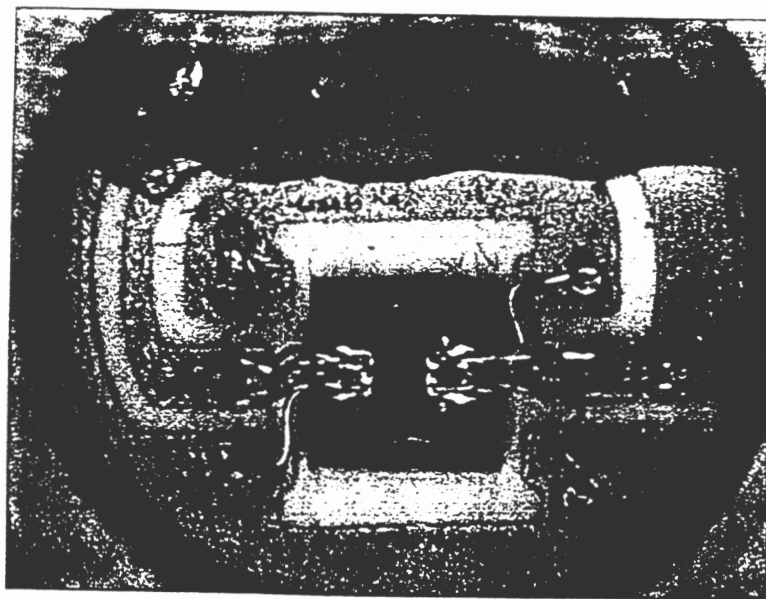
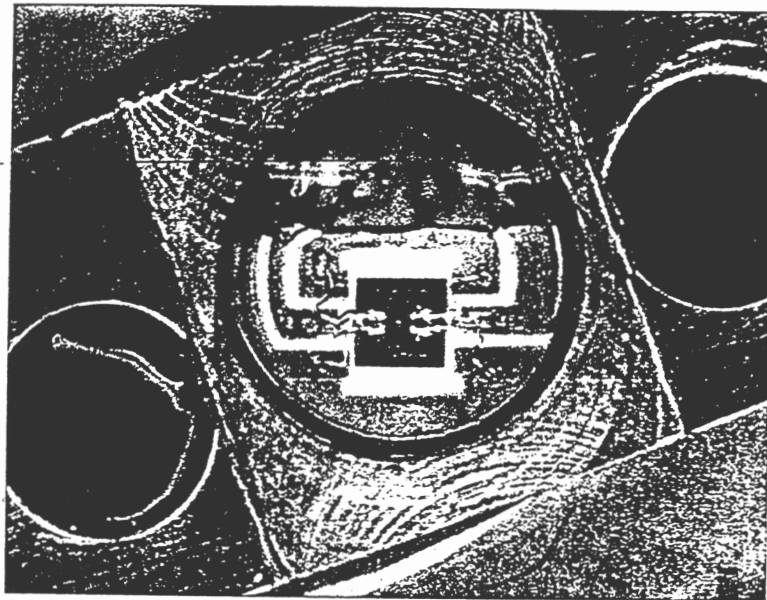


Fig. 1 Micrographs of "opened" 7270A revealing die bonding orientation and die layout.



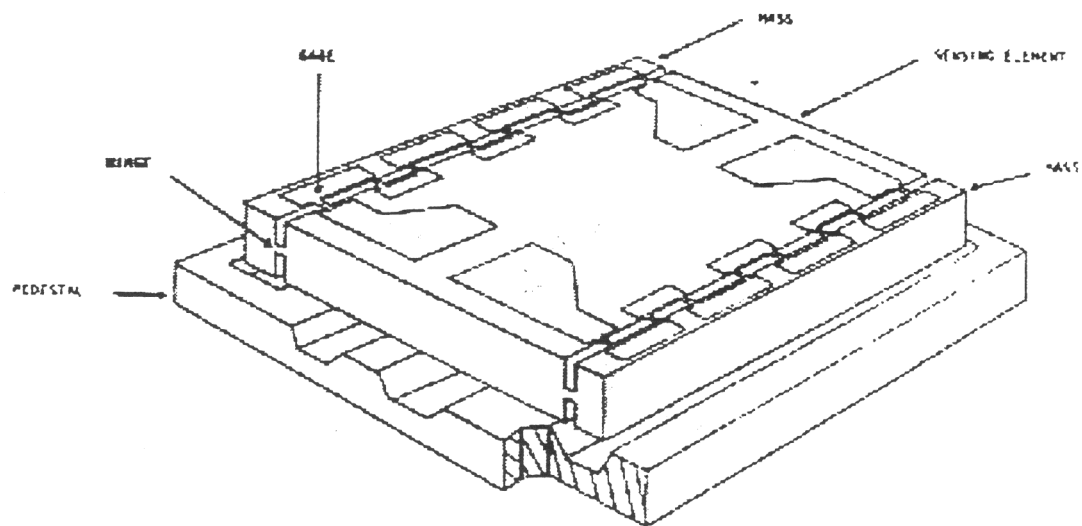


Fig. 2 Perspective drawing of monolithic silicon construction of Endevco 7270A [3].

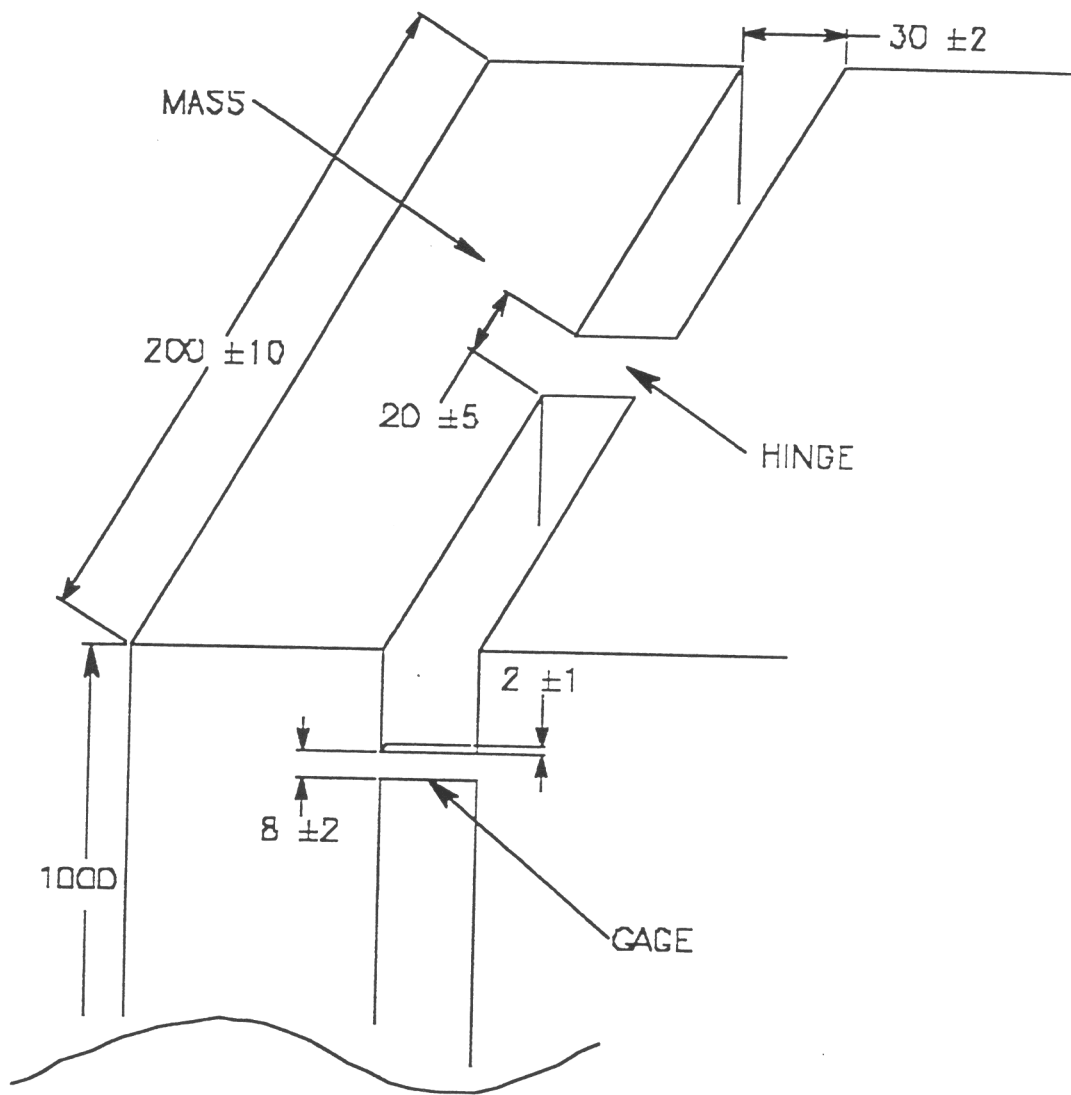


Fig. 3 Drawing of 7270A hinged proof mass and gage showing approximate dimensions for the  $\pm 200,000$  g device.

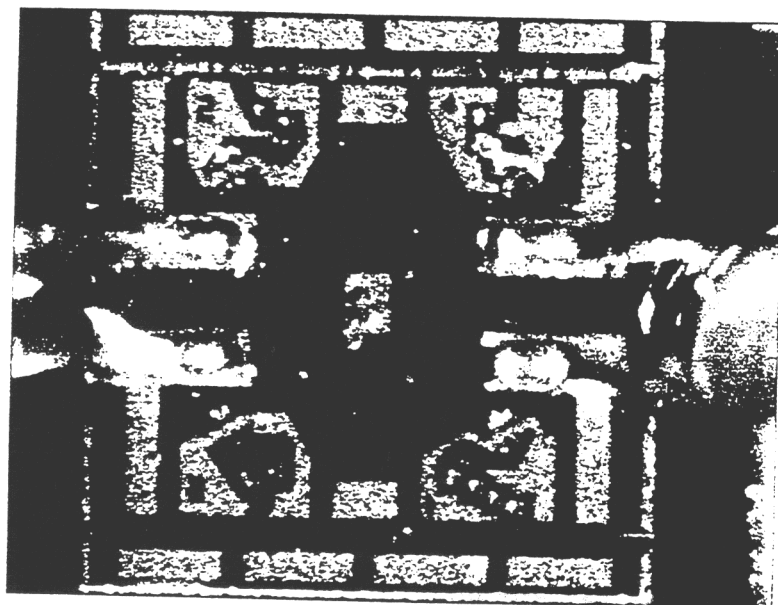


Fig. 4 Micrograph of good device showing resistor layout, proof masses, and piezoresistor bridges.



Fig. 5 Micrographs of broken devices received from Eglin AFB. In a) corner of silicon proof mass is chipped. In b) both proof masses have broken off.

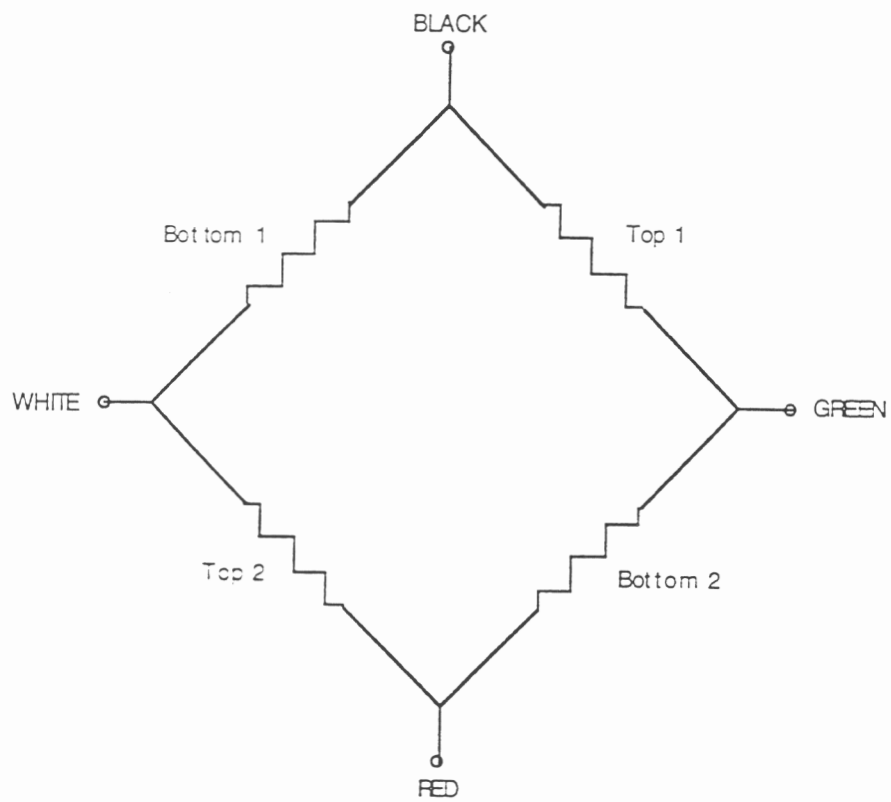


Fig. 6 Electrical connection of 7270A showing location of resistors on die relative to leads.

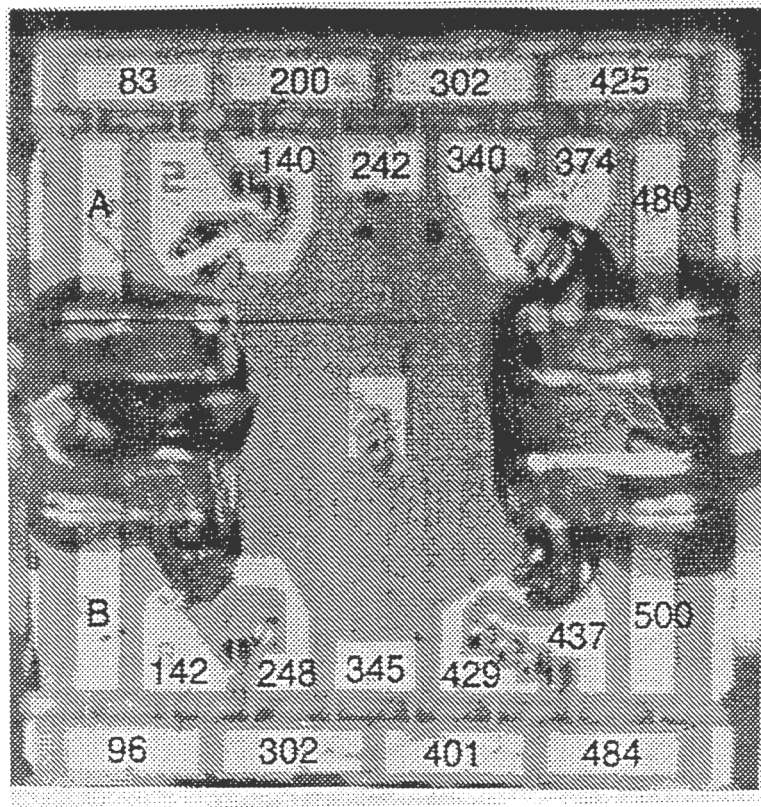


Fig. 7 Resistor map of a good device. The pad numbers indicate resistance values in ohms measured on each pad with respect to pads A or B (e.g. the total resistance of resistor arm A is 480 ohms). The measurement error is roughly  $\pm 5$  ohms due to variable probe contact resistance.



Fig. 8 Optical photograph of good die mapped in Fig. 7. The use of breakout resistor trimming is evident in three areas on the die.

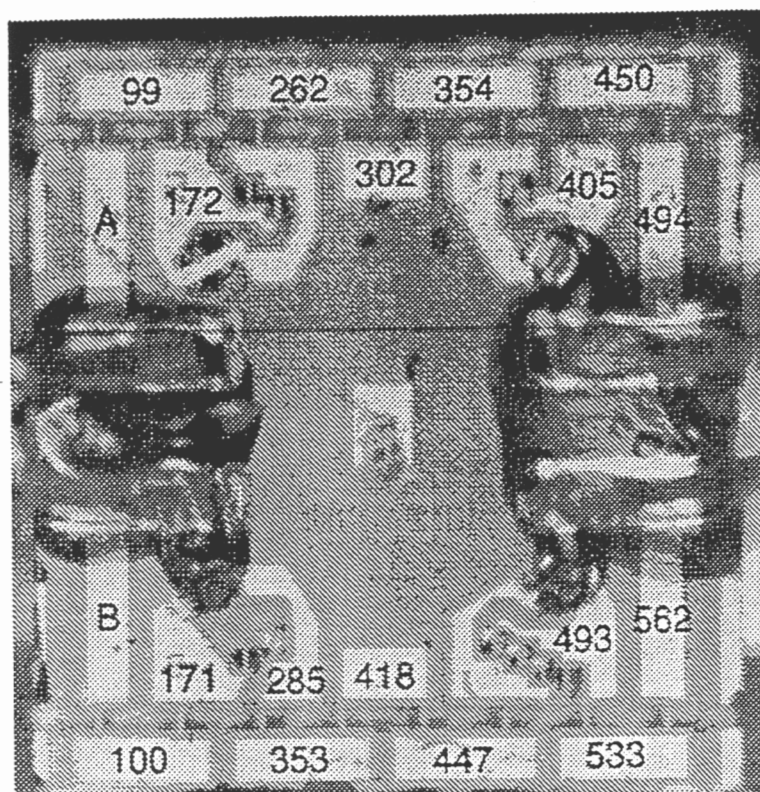


Fig. 9 Resistor map of failed device.



Fig. 10 Optical photograph of device in Fig. 9.



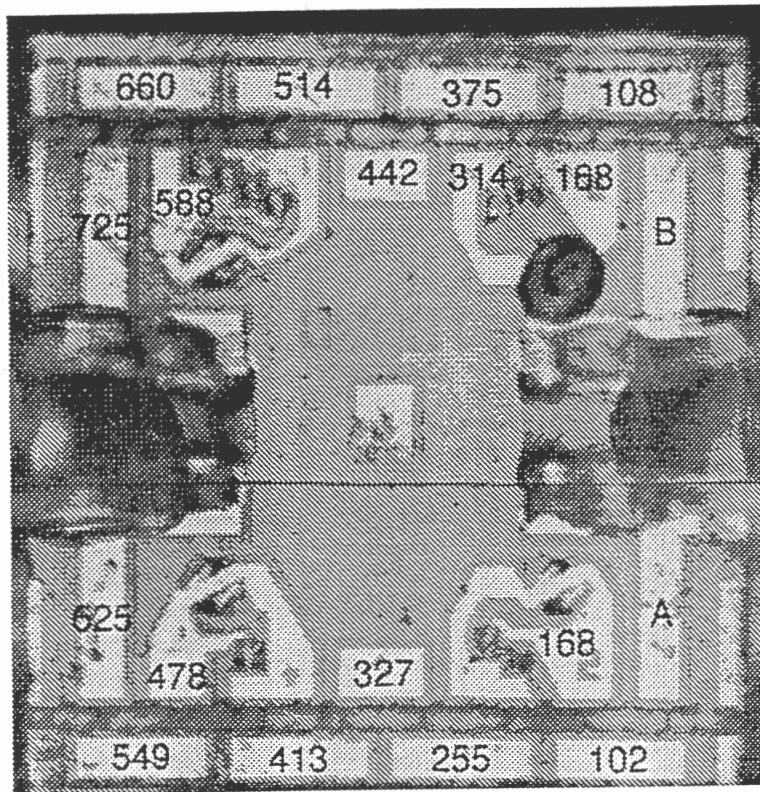


Fig. 11 Resistor map of failed device.

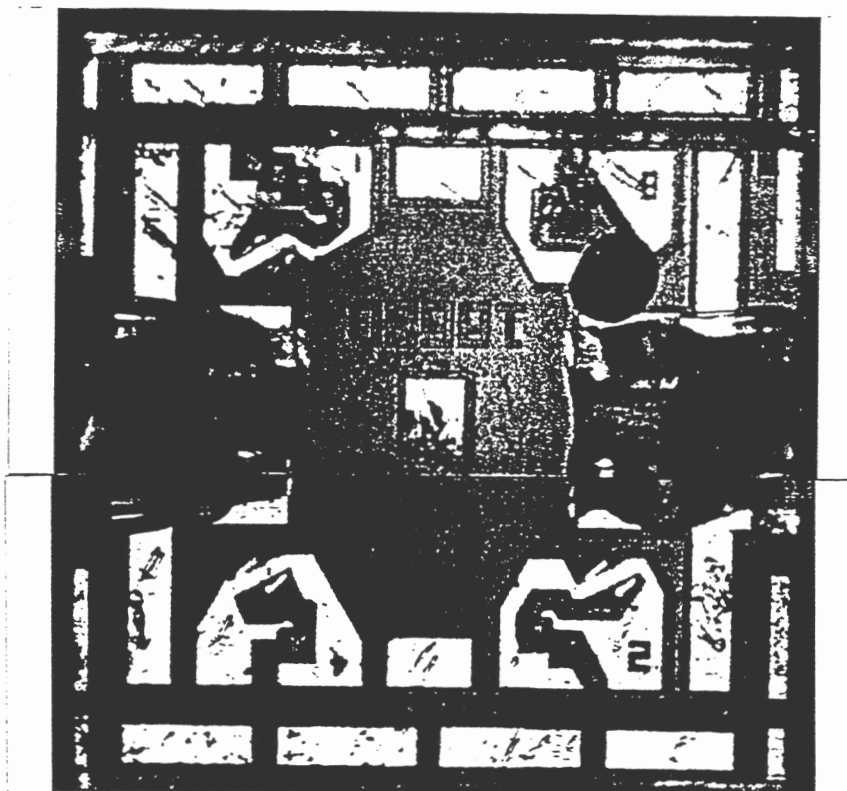


Fig. 12 Optical photo of device in Fig. 11.

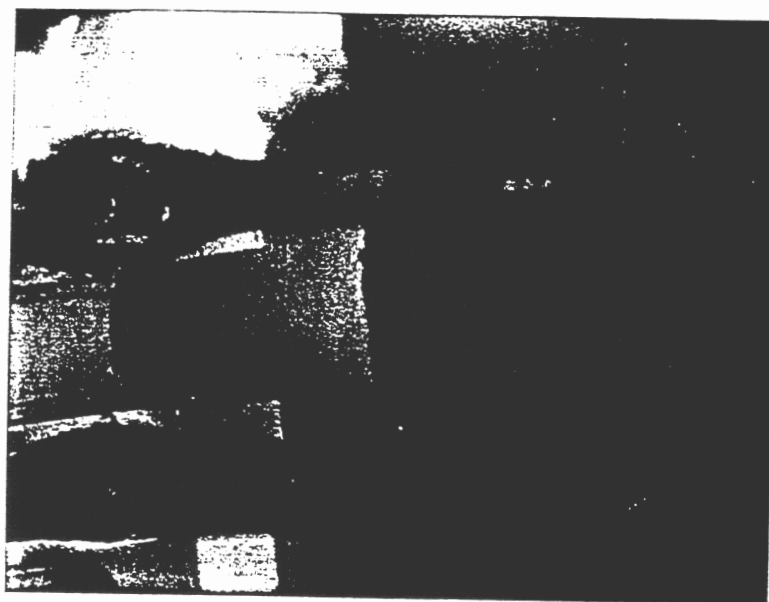
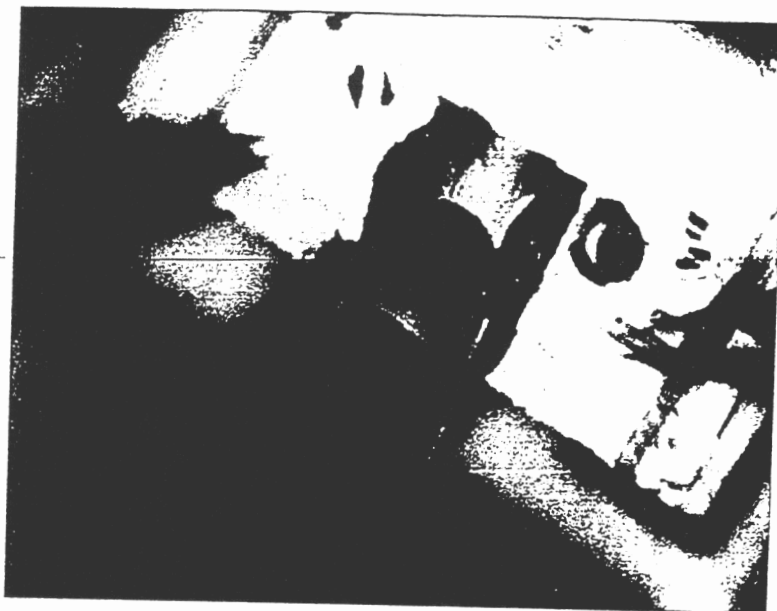


Fig. 13 Optical photograph of separated bonding wires for device in Fig. 12.

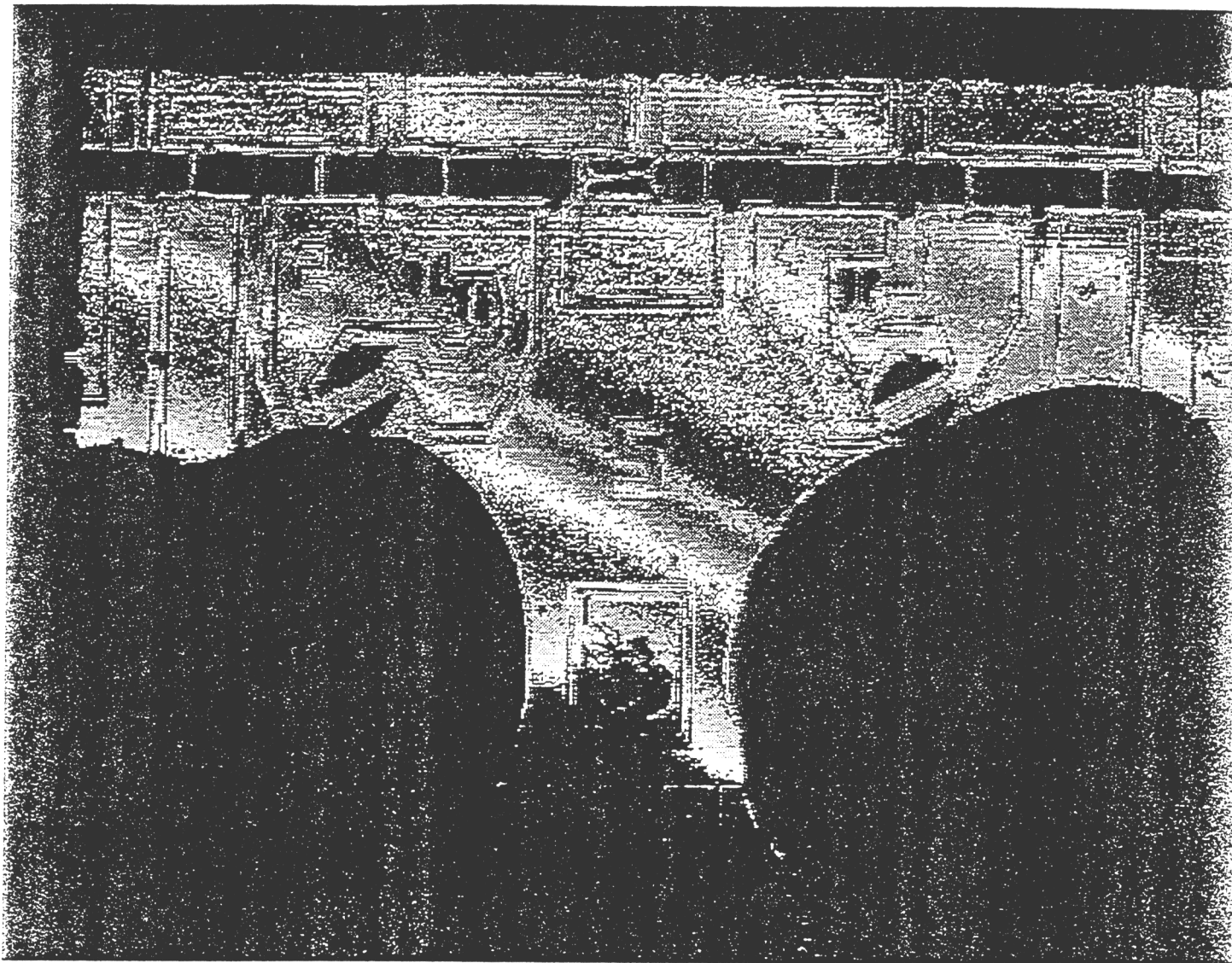


Fig. 14

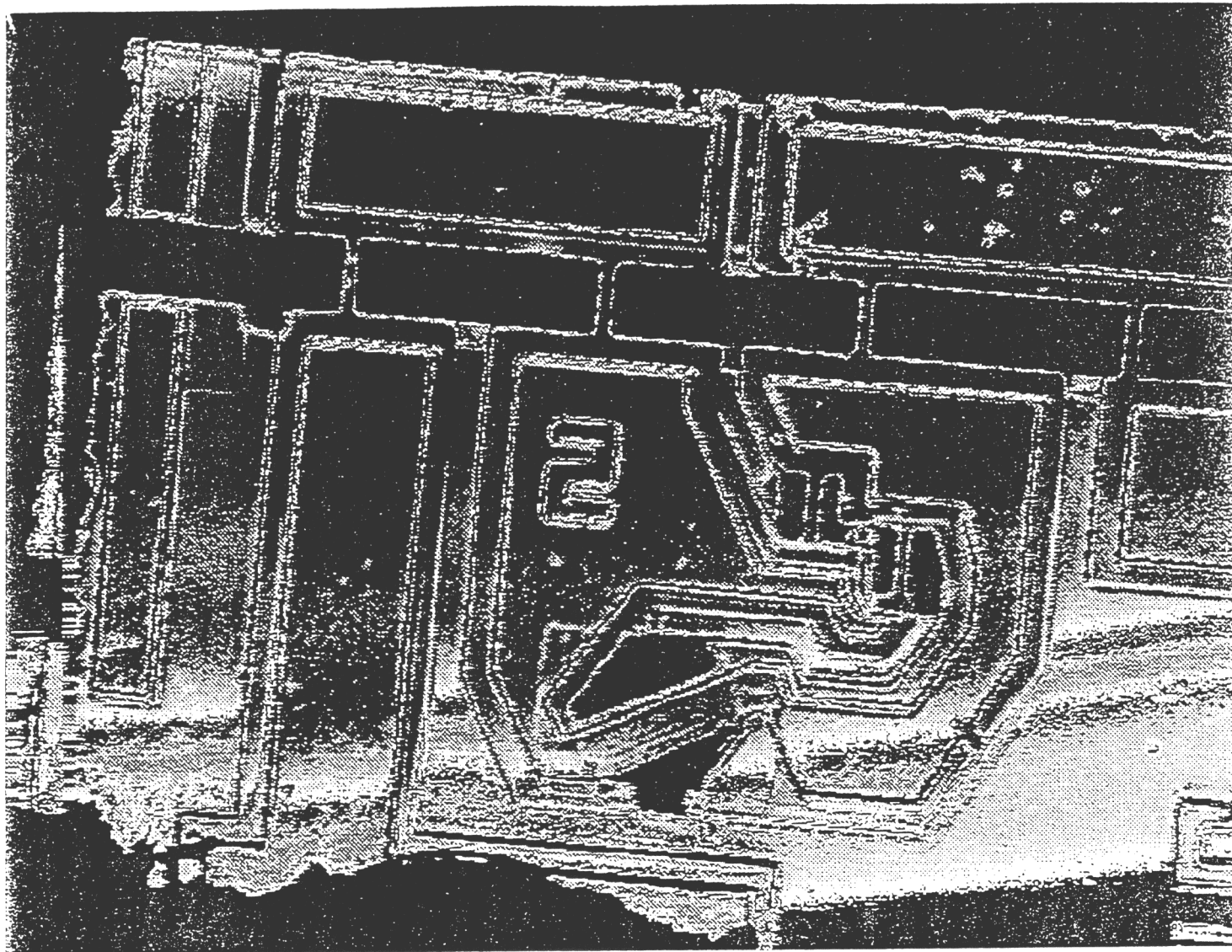


Fig. 14

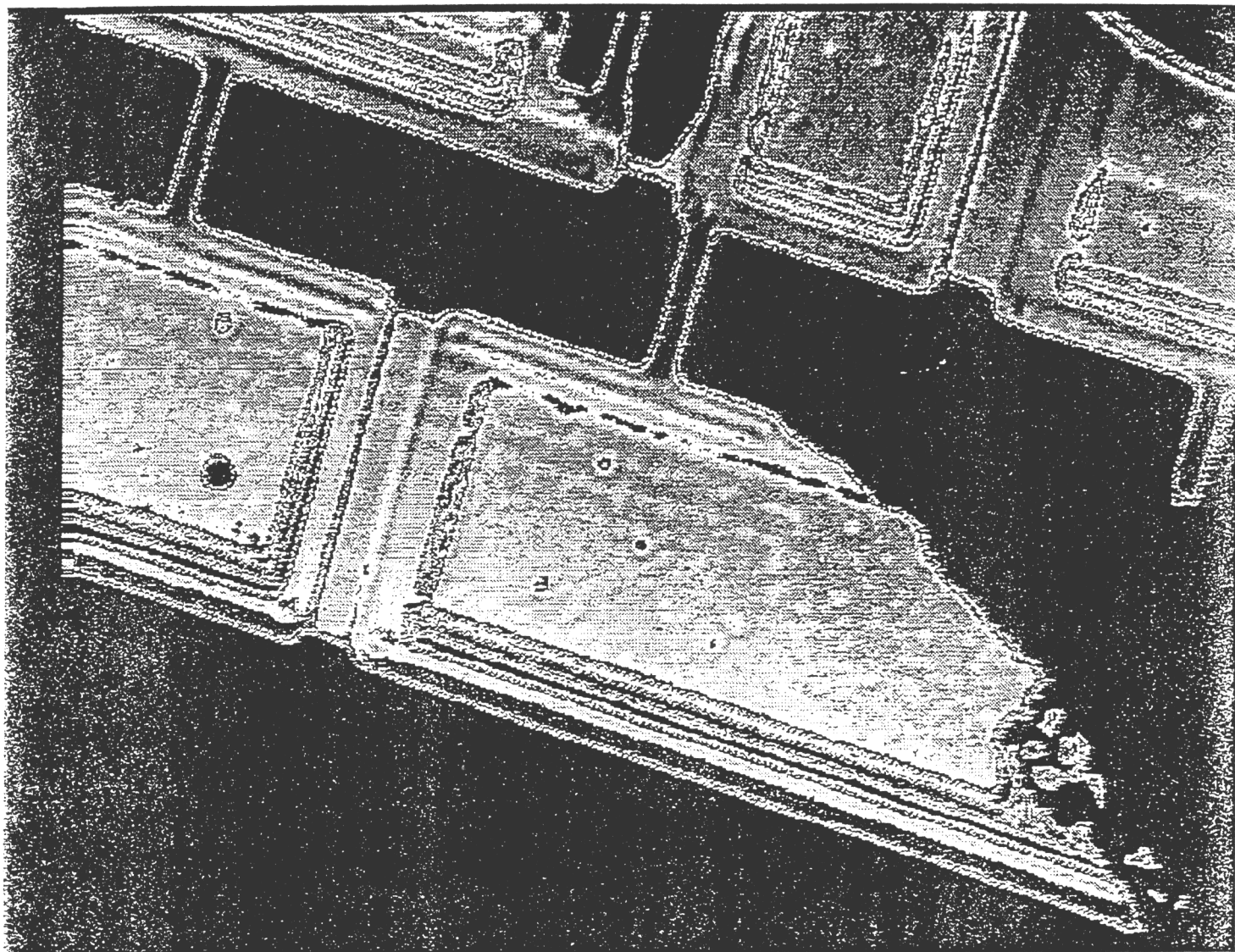


Fig. 14



◆ ALGOR-V

LOAD CASE

First

Prev

Next

Case num

-----  
Scal calc  
-----

[Esc]

1Help 2Undo

3Inp 4Snap

5Cur 6Swfc

7Big 8Menu

9Top 0Draw

Mode 1: 0 Frequency = 4928256.5000 (rad/time) 784356.3837 (cycles/time)

File:accel51

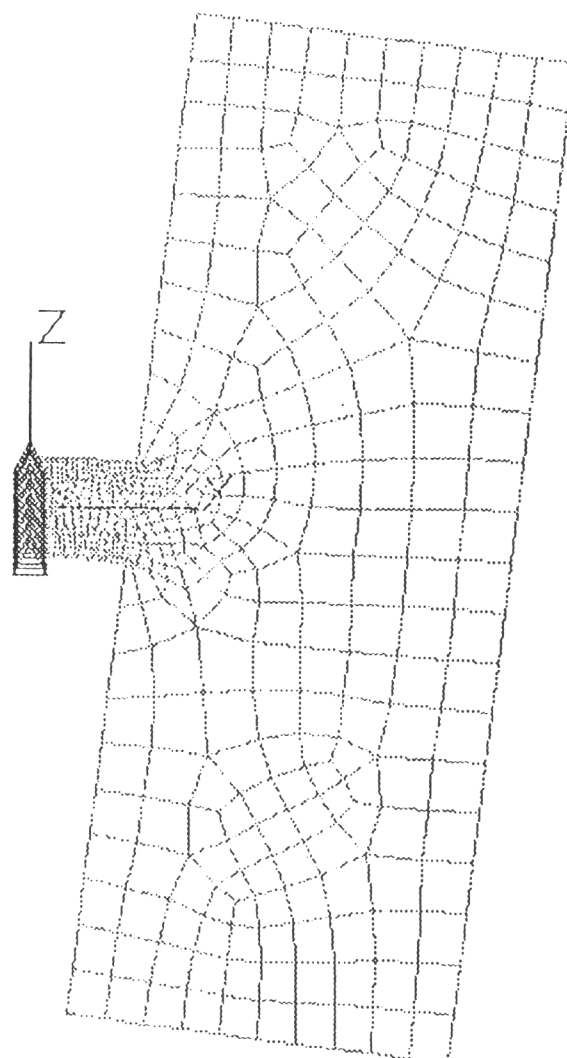
S=N LC 1/ 5

Vu= 5

X= 0.0000

Y=-113.79

Z=34.5978



◆ ALGOR-V

LOAD CASE

First

Prev

Next

Case num

Scal calc

[Esc]

1Help 2Undo

3Inp 4Snap

5Cur 6Swtc

7Big 8Menu

9Top 0Draw

Mode 2: 0 Frequency = 36981796.0000 (rad/time) 5885835.6445 (cycles/time)

File:accal51

S=N LC

2/ 5

Vu= 5

X= 0.0000

Y=-159.11

Z=70.6058

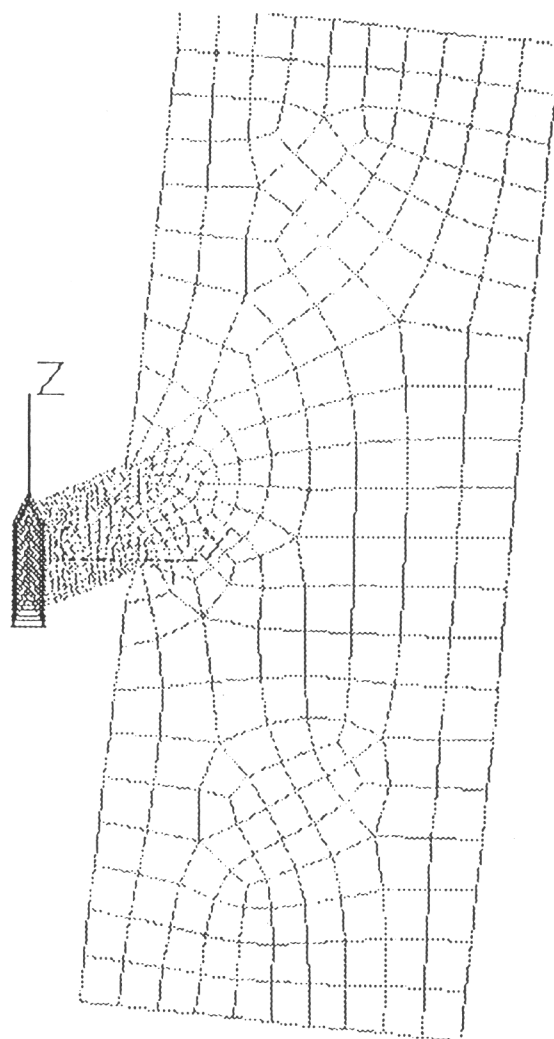


Fig. 15

◆ ALGOR-V

LOAD CASE

First

Prev

Next

Case num

Scale calc

[Esc]

1Help 2Undo

3Inp 4Snap

5Cur 6Swfc

7Blg 8Menu

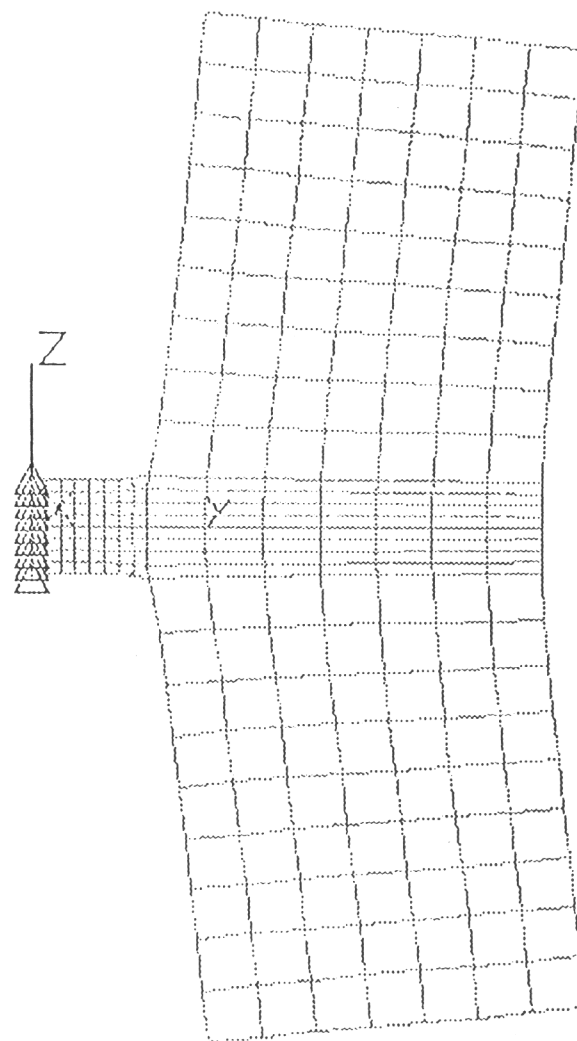
9Top 0Draw

Mode 3: 0 Frequency = 43979700.0000 (rad/time) 6999586.6587 (cycles/time)

File:accel4 S=N LC 3/ 5 Vu= 5 X= 0.0000

Y=-108.28

Z=61.7097





## DISTRIBUTION

5	1080	B. Davies, 1325
1	0555	V. Bateman, 9742
1	0555	F. Brown, 9742
1	1082	R. Chanchani, 1333
1	0329	T. Christenson, 2643
1	1080	S. Montague, 1325
1	1072	J. Murray, 1274
1	0987	D. Rey, 2664
5	0987	D. Ryerson, 2664
1	1080	J. Smith, 1325
1	9018	Central Library Files, 8940-2
2	0899	Technical Library, 4916
2	0619	Review and Approval Desk, 12690 for DOE/OSTI
2	0188	LDRD Office, 4523